Theor Chem Account (2008) 121:123–134
DOI 10.1007/s00214-008-0455-2

REGULAR ARTICLE

Theoretical studies on the electronic structures and spectroscopic properties for a series of Osmium(II)-2,2′,6′,2″-terpyridine complexes

Jian-Po Zhang · Xin Zhou · Tao Liu · Fu-Quan Bai · Hong-Xing Zhang · Au-Chin Tang

Received: 19 December 2007 / Accepted: 2 May 2008 / Published online: 21 May 2008

Abstract A series of Osmium(II) complexes [Os(trpy-R)$_2$]$^{2+}$(trpy=2,2′,6′,2″-terpyridine and R=H (**1**), OH (**2**), and C_6H_5(**3**)) have been investigated by the density functional (DF) and ab initio calculations. The structures of **1–3** in the ground and excited states were fully optimized at the B3LYP and CIS level, respectively, and their absorption and emission spectra in the acetonitrile solution were obtained using the TD-DFT (B3LYP) method associated with the PCM model. The calculations indicated that, for **1–3**, the variation of the substituents on the terpyridine ligand only slightly changes their geometrical structures in the ground and excited states but leads to a sizable difference in the electronic structures. The results show that the low-lying MLCT/ILCT transitions (at 446 (1), 465 (2), and 499 nm (3)) are red-shifted according to the electron-donating ability of substituents on the terpyridine ligand, but blue-shift trend of the high-lying ILCT transitions (at 301 (1), 297 (2), and 272 nm (3)). It also reveals that the lowest energy emissions of **1–3** at 649 nm, 656 nm, and 676 nm have the character of mixing $^3[\pi^*(\text{trpy}) \rightarrow \text{d(Os)}]$ and $^3\pi\pi^*$ (^{3}MLCT/^{3}ILCT) transitions localized on the terpyridine ligand, which are identical to the transition properties of the lowest-energy absorptions.

Keywords Osmium(II) complexes · Electronic structures · Spectroscopic properties · TD-DFT calculations · CIS methods

1 Introduction

Transition metal complexes of Osmium(II) have drawn the research interests from both experimental and theoretical views in the past decades [1–12], because they hold a large number of fascinating photochemical characters such as UV/Vis absorption, photoluminescence, and long-lifetime emission [9]. Most characters are ascribed to the imposed strong spin-orbit coupling induced by Os atom, which can effectively promote singlet-to-triplet intersystem crossing and enhance the consequent radiative transition from the triplet state to the single state [13,14]. Therefore, Osmium(II) complexes have been widely applied in solar energy conversion, luminescence sensing, electroluminescence and/or phosphorescent organic light-emitting diodes (OLEDs) [15–26].

Attentions were once focused on a series of simple bidentate complexes such as [Os(orRu)(bpy)$_3$]$^{2+}$ (bpy=2,2′-bipyridine), because of its unique chemical stability, redox properties, strong luminescence intensities and long excited state lifetimes [27–30]. But the bidentate complexes of Ru and Os are not suitable for the construction of supramolecular systems from geometric viewpoint [31], several research groups have paid much attention to the tridentate Os and Ru complexes [32–39], such as [Os(orRu)(trpy)$_2$]$^{2+}$ [40], since the tridentate ligand has predominant structural advantages on the formation of supramolecular systems. Several [Ru(trpy-X)(trpy-Y)]$^{2+}$ complexes (X or Y=$MeSO_2$, Cl, H, Ph, EtO, OH, or Me_2N) have been investigated experimentally by Mauro et al. [41]. The absorption spectra shows

Electronic supplementary material The online version of this article (doi:10.1007/s00214-008-0455-2) contains supplementary material, which is available to authorized users.

J.-P. Zhang · X. Zhou · T. Liu · F.-Q. Bai · H.-X. Zhang (✉) · A.-C. Tang
State Key Laboratory of Theoretical and Computational Chemistry, Institute of Theoretical Chemistry, Jilin University, 130023 Changchun, People's Republic of China
e-mail: zhanghx@jlu.edu.cn

that spin-allowed metal-to-ligand charge-transfer (^{1}MLCT) absorption is in the visible spectral region, and the complexes show intense luminescence in the solid state, with lifetimes in the 1–10 μs scale.

Recently, Philippe et al., and Ciofini et al. studied a series of novel tridentate complexes: $[(ttrpy)Os(trpy\text{-}ph\text{-}TPH_3^+)]^{3+}$, $[(ttrpy)Os(trpy\text{-}xy\text{-}TPH_3^+)]^{3+}$, $[(ttrpy)Os(trpy\text{-}ph\text{-}TPH_2(NO_2)^+)]^{3+}$, and $[(ttrpy)Os(trpy\text{-}xy\text{-}TPH_2(NO_2)^+)]^{3+}$ (TP^+=2,4,6-triarylpyri-dinium) in terms of designing photochemical molecular devices (PMDs) [42–45]. The complexes are all P–A-type dyads, which are made of Os(II) bis-trpy as the photosensitizer (P) and TP^+ group as the electron acceptor (A), and the dyads can form charge-separated (CS) states upon light excitation. Specially, the photosensitizer part for $[Os(trpy)_2]^{2+}$ plays an important role in the CS process [46]. These CS excited states actually correspond to the transient conversion of light into an electrochemical potential, which can be potentially used either for energy storage or for electricity production [47–51]. Each components of the polyads has been the subject of intense experimental design and synthetic work, aiming at identifying and selecting the best P, A and D (electron donating) building blocks as well as proposing satisfactory intercomponent bridging units.

Although there are many experimental researches on the photophysical and photochemical properties of luminescent $[Os(trpy)_2]^{2+}$ complexes, the theoretical studies of the Os(II) bis-trpy on their electronic structures and spectroscopic properties are scarce. Recently, Zhou [52] calculated a series of terpyridyl Ru and Os complexes, in which the works were focused on the description of Ru(II) terpyridine complexes, but the substituent Os(II) terpyridine complexes were less studied. It is well known that the spectroscopic and geometrical properties for Os(II) may be of significant difference compared with Ru(II) due to the discrepancy in the relativistic effect of 4d and 5d electrons. Therefore, a deep insight into the structures and spectroscopic properties for this kind of complexes is much needed and significant. The present work aims at determining the substituents effects on the electronic structures and spectroscopic properties of these complexes, and assess the validity of the generally accepted [1–12,14] MLCT transition for the lowest-energy absorption and emission. We hope that the theoretical investigations can provide an important clue in designing the novel transition metal complexes and improving the photosensitizer candidate in term of PMDs. Herein, we performed theoretical calculations on $[Os(trpy\text{-}R)_2]^{2+}$ (trpy=2,2′,6′,2″-terpyridine and R=H (**1**), OH (**2**), and C_6H_5(**3**)) complexes in the ground and excited states using ab initio and density functional theory (DFT) methods. The calculations indicated that the ^{3}MLCT/^{3}ILCT transitions are responsible for the lowest-energy phosphorescence of **1**–**3** and the phosphorescent emissions are red-shifted as the increasing of the ability of electron-donating of substituents.

2 Computational details and theory

The Becke's three parameter functional and the Lee–Yang–Parr functional (B3LYP) [53] and single-excitation configuration interaction (CIS) methods [54–56] were employed to optimize the ground and excited-state structures of **1**–**3**, respectively. On the basis of the optimized structures in ground and excited states, the spectroscopic properties related to the absorption and emission in acetonitrile were obtained by the time-dependent density functional theory (TD-DFT) [57–59] at B3LYP functional associated with the polarized continuum model (PCM) [60,61].

The complexes investigated here are shown in Fig. 1. The calculated complexes display D_{2d} symmetry for **1** and C_2 symmetry for **2** and **3** in both the ground and excited states. The orientation of the complexes in Cartesian coordinates is also displayed in Fig. 1. In the calculations, quasirelativistic pseudopotentials of the Os atoms proposed by Hay [62] and Wadt [63] with 16 valence electrons were employed, and the LANL2DZ basis sets associated with the pseudopotential were adopted. The basis sets were described as Os (8s6p3d/3s3p2d), C, N and O (10s5p/3s2p), and H (4s/2s). Therefore, 390 basis functions and 258 electrons for **1**, 408 basis functions and 274 electrons for **2**, 514 basis functions and 338 electrons for **3** are included in the calculations. All

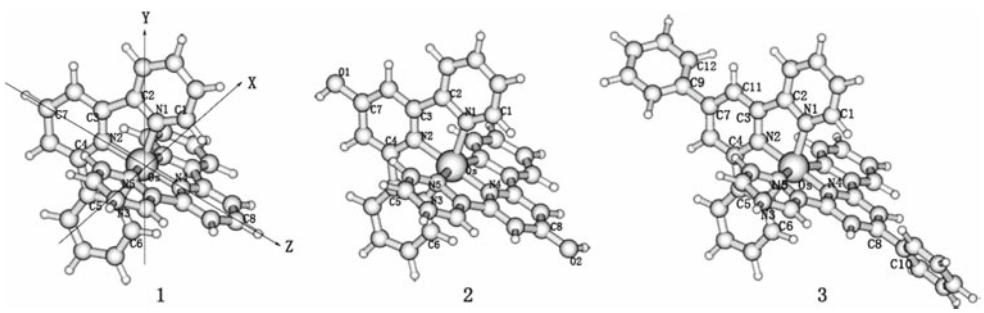

Fig. 1 Optimized geometry structures of **1**–**3** at the B3LYP/LANL2DZ level

Table 1 Main optimized geometry structural parameters of the complexes in the ground and lower lying triplet excited states at the B3LYP and CIS levels, respectively, together with the experimental values of **1**

Parameter	1		2		3		
	X^1A	A^3A	X^1A	A^3A	X^1A	A^3A	1 Expt[a]
Bond lengths (Å)							
Os-N(1)	2.100	2.132	2.099	2.157	2.100	2.156	2.089
Os-N(2)	2.010	2.035	2.015	2.039	2.010	2.057	1.972
Os-N(3)	2.100	2.132	2.101	2.161	2.100	2.156	2.089
N(1)-C(1)	1.360	1.343	1.360	1.329	1.360	1.333	
N(1)-C(2)	1.388	1.366	1.389	1.371	1.388	1.358	
N(2)-C(3)	1.373	1.350	1.369	1.352	1.371	1.336	
N(2)-C(4)	1.373	1.350	1.374	1.348	1.373	1.336	
C(7)-O(1)			1.365	1.352			
Bond angles (deg)							
N(1)-Os-N(2)	78.4	77.9	78.1	77.7	78.2	77.7	78.9
N(3)-Os-N(2)	78.4	77.9	78.3	77.7	78.2	77.7	
N(2)-Os-N(4)	180.0	180.0	179.8	179.9	180	180	
N(3)-Os-N(4)	101.6	102.1	101.8	102.2	101.8	102.3	
N(1)-Os-N(4)	101.6	102.1	101.7	102.3	101.8	102.3	
Dihedral angles (deg)							
N(1)-Os-N(2)-N(5)	–90.0	–90.0	–90.3	–89.9	–90.4	–89.9	
C(11)-C(7)-C(9)-C(12)					34.42	42.0	

[a] From refs. [40] and [43]

the calculations are accomplished by using the Gaussian03 (Revision C.02) program package [64] on an origin/3900 server.

3 Results and discussion

3.1 The ground-state structures and absorption spectra in the CH_3CN solution

The ground-state structures of **1**–**3** are fully optimized by the B3LYP method. The calculated results reveal that all of the complexes have the X^1A ground state. The optimized structures are illustrated in Fig. 1, and the corresponding main geometrical parameters together with the X-ray crystal diffraction data of **1** [40,43] are listed in Table 1. It shows that the two trpy planes are almost perpendicular to each other with N(1)-Os-N(2)-N(5) dihedral angles very close to 90°. Furthermore the optimized bond lengths and bond angles of all the complexes in the ground state are in general agreement with the corresponding experimental values of **1**. The calculated bond distances of Os-N(1) (2.100 Å), and Os-N(2) (2.010 Å) are slightly longer by about 0.01–0.04 Å compared with the measured values. The bond angles of N(1)-Os-N(2) of **1** are about 78.4°, corresponding well to the experimental values of 78.9°. The distance of N(2)-C(3) of **1**–**3** is ca. 1.37 Å, which is much shorter than a normal N-C single bond length of 1.48 Å, indicating some delocalization of the lone pairs of the central amine nitrogens into the pyridine rings. The dihedral angle of C(11)-C(7)-C(9)-C(12) of **3** is about 34.4°, it is in favor of forming the π-conjugation between the phenyl and terpyridine. Therefore, phenyl would act as a strong electron donator in complex **3** when needed.

The calculated absorptions in the UV-visible region associated with their oscillator strengths, the main configurations and their assignments, and the experimental results are summarized in Table 2; the frontier molecular orbital compositions of **1**–**3** are compiled in Tables 3, 4, and 5, respectively, Fitted Gaussian type absorption curves with the calculated absorption data are shown in Figs. 3 and 4. To intuitively understand the transition process, we display the electron density diagrams of **1** in Fig. 2, in Figs. S1 and S2 (Supporting Information) for **2** and **3**, respectively, and the molecular orbital energy levels involved in the transitions of **1**–**3** are displayed in Fig. 5.

With respect to **1**, as seen in Table 2, four low-lying dipole-allowed absorptions at 547, 446, 301, and 243 nm are attributed to the MLCT/ILCT, MLCT/ILCT, ILCT/LMCT, and ILCT/LMCT transitions, respectively. In view of the D_{2d} symmetry of **1**, there are some degenerate orbitals such as MOs 33e, 34e, 35e, 36e and 37e. In Table 3, higher occupied

Table 2 Absorptions of **1–3** in acetonitrile under TD-DFT (B3LYP) calculations, together with experimental values

	Transition	Config (CI coeff)	E, nm (ev)	Oscillator	Assignment	λ_{exptl} (nm)[a]
1	$X^1A_1 \rightarrow A^1E$	$5b_1 \rightarrow 35e$ (0.69)	547.34 (2.27)	0.0196	MLCT/ILCT	536
	$X^1A_1 \rightarrow B^1B_2$	$5b_1 \rightarrow 5a_2$ (0.52)	446.23 (2.78)	0.2505	MLCT/ILCT	477
	$X^1A_1 \rightarrow C^1E$	$4b_1 \rightarrow 35e$ (0.63)	301.48 (4.11)	0.4777	ILCT/LMCT	312
	$X^1A_1 \rightarrow D^1E$	$33e \rightarrow 35e$ (0.49)	243.18 (5.10)	0.4941	ILCT/LMCT	270
2	$X^1A_1 \rightarrow A^1B$	68a→69b (0.54)	533.56 (2.32)	0.0204	MLCT/ILCT	
	$X^1A_1 \rightarrow B^1B$	68a→70b (0.40)	465.23 (2.67)	0.2519	MLCT/ILCT	
		68a→69b (−0.34)			MLCT/ILCT	
	$X^1A_1 \rightarrow C^1B$	67b→70a (0.67)	297.20 (4.17)	0.2573	ILCT/LMCT	
	$X^1A_1 \rightarrow D^1B$	66b→70a (0.34)	261.79 (4.74)	0.1452	LLCT/LMCT	
		66a→69b (0.28)			LLCT/ILCT	
3	$X^1A_1 \rightarrow A^1B$	89a→81b (0.67)	550.21 (2.25)	0.0176	MLCT/ILCT	
	$X^1A_1 \rightarrow B^1A$	79b→81b (0.30)	499.25 (2.48)	0.1920	MLCT/ILCT	490
		80b→81b (0.30)			MLCT/ILCT	
	$X^1A_1 \rightarrow C^1A$	78b→81b (0.49)	311.80 (3.98)	0.1815	LLCT/LMCT	314
		77b→82b (0.48)			LLCT/LMCT	
	$X^1A_1 \rightarrow D^1A$	86a→91a (0.54)	272.03 (4.56)	0.7933	ILCT/LMCT	286

[a] From refs. [40] and [44]

Table 3 Molecular orbital compositions related to the absorption for $[Os(tpy\text{-}H)_2]^{2+}$(**1**) at the B3LYP level

Orbital	Energy (eV)	Composition (%)		Assignment of orbitals
		Os	trpy	
$27b_2$	0.1192	50.1	49.9	π^*(trpy)+d_{xz}(Os)
37e	−0.5845		96.9	π^*(trpy)
$7b_1$	−1.1410	9.1	90.9	π^*(trpy)+d_{xy}(Os)
36e	−1.4904		97.9	π^*(trpy)
$6a_2$	−1.5780		100.0	π^*(trpy)
$6b_1$	−2.2899		93.9	π^*(trpy)+d_{xy}(Os)
$5a_2$	−2.4444		100.0	π^*(trpy)
35e	−2.5889	12.9	87.1	π^*(trpy)+$d^2_{x-y}{}^2$(Os)
HOMO-LUMO energy gap				
$5b_1$	−5.7846	67.3	32.7	d_{xy}(Os)+π(trpy)
34e	−5.9202	64.6	35.4	d_{yz}(Os)+π(trpy)
$4a_2$	−7.1860		100.0	π (trpy)
$4b_1$	−7.2451		96.9	π (trpy)
33e	−8.1172		98.1	π (trpy)

MOs ($5b_1$, 34e) are comprised of substantial compositions of metal Os(II) atom, while the terpyridyl ligand dominates the virtual MOs (35e, $5a_2$). With respect to the 547 nm lowest-energy absorption, the $5b_1 \rightarrow 35e$ excitation corresponds to the largest CI coefficient of 0.69. As seen in Table 3, MO $5b_1$ is the highest occupied MO (HOMO) composed of about 67% metal Os(II) and 33% terpyridyl ligand, while the lowest unoccupied MO 35e (LUMO) lies above the HOMO by about 3.2 eV, is mainly localized on the terpyridyl ligand with the 87% composition. Therefore, the lowest-energy absorption at 547 nm with oscillator strength of 0.0196 arising from the $X^1A_1 \rightarrow A^1E$ transition is assigned as the Os(II)+π(trpy) → π^*(trpy) charge transfer (MLCT/ILCT) transition. The lowest-energy absorption is coincided with the 537 nm absorption in experiments, but the oscillator strength is so small that can obviously be observed for the cases of **2** and **3** in experiments [40,43,44]. For the 446 nm absorption from the $X^1A_1 \rightarrow B^1B_2$ transition, the

Table 4 Molecular orbital compositions related to the absorption for $[Os(tpy\text{-}OH)_2]^{2+}$(**2**) at the B3LYP level

		Composition (%)			
Orbital	Energy (eV)	Os	trpy	OH	Assignment of orbitals
70b	−2.4281	7.3	91.3		π^*(trpy) + d_{xz}(Os)
70a	−2.4488	11.4	86.8		π^*(trpy) +$d^2_{x-y}{}^2$(Os)
69b	−2.4621		94.7		π^*(trpy)
HOMO-LUMO energy gap					
69a	−5.6589	63.9	33.2		d_{xy}(Os) + π(trpy)
68b	−5.6606	61.1	34.1		d_{yz}(Os) + π(trpy) + P_x
68a	−5.6777	64.3	33.6		d^2_z(Os) + π(trpy)
67b	−7.2018		99.7		π(trpy)
67a	−7.2492		97.3		π(trpy)
66a	−7.8571		57.3	37.3	π(trpy)+P_z
66b	−7.8573		57.4	37.3	π(trpy)+P_x

Table 5 Molecular orbital compositions related to the absorption for $[Os(tpy\text{-}C_6H_5)_2]^{2+}$(**3**) at the B3LYP level

		Composition (%)			
Orbital	Energy (eV)	Os	trpy	C_6H_5	Assignment of orbitals
91a	−2.2869		89.5		π^*(trpy)
90a	−2.4420		95.6		π^*(trpy)
82b	−2.6033	13.0	83.2		π^*(trpy) + $d^2_x{}^2_y$(Os)
81b	−2.6066	13.0	83.2		π^*(trpy) + d_{xz}(Os)
HOMO-LUMO energy gap					
89a	−5.7743	67.2	32.5		d_{xy}(Os) + π (trpy)
80b	−5.8026	59.6	33.8		d_{yz}(Os) + π (trpy)
79b	−5.8070	59.7	33.8		d^2_z(Os) + π (trpy)
78b	−7.0538		22.5	69.2	$\pi(c_6h_5) + \pi$ (trpy)
77b	−7.0581		22.4	69.3	$\pi(c_6h_5) + \pi$ (trpy)
88a	−7.1354		7.9	92.1	$\pi(c_6h_5) + \pi$ (trpy)
87a	−7.1368			95.7	$\pi(c_6h_5)$
86a	−7.1969		94.7		π(trpy)

$5b_1 \rightarrow 5a_2$ excitation corresponding to the largest CI coefficient of 0.52 dominates the absorption. As indicated in Table 3, MO $5a_2$, ∼0.15 eV higher than 35 e (LUMO), is pure terpyridyl π-bonding orbital. Thus, the absorption at 446 nm is attributed to the Os(II) + π(trpy) → π^*(trpy) charge transfer (MLCT/ILCT) transition with a larger oscillator strength of 0.2505. With regard to the C^1E excited state, the 301 nm absorption is mainly contributed from the $4b_1 \rightarrow$ 35e excitation (CI coefficient = 0.63). Among the four low-lying absorptions, the 301 nm absorption with the oscillator strength of 0.47 is considered as the most intense absorption observed in experiments. From Table 3, the MO $4b_1$ (HOMO-3) is mainly localized on the terpyridyl ligand with the 97% composition. We can attribute the lower-lying absorption at 301 nm to the ILCT/LMCT character, which corresponds to the lower-energy absorption at 312 nm in experiments. In the $X^1A_1 \rightarrow D^1E$ transition, the 33e → 35e excitation corresponding to the largest CI coefficient of 0.49 dominates the absorption. As depicted in Table 3, the MO 33e are pure terpyridyl based involving substantial terpyridyl (ca. 98%) and the MO 35e are localized on ligand terpyridyl (ca. 87%) perturbed by some metal Os(II) contribution (ca. 13%), so the 243 nm absorption is assigned to the ILCT transition within mixed with some LMCT characters.

To intuitively understand the absorption of **1** in solution, we display the electron density diagrams in Fig. 2, in which involved four single electron excitations corresponding to the maximal CI coefficients. Fig. 2 could help to comprehend

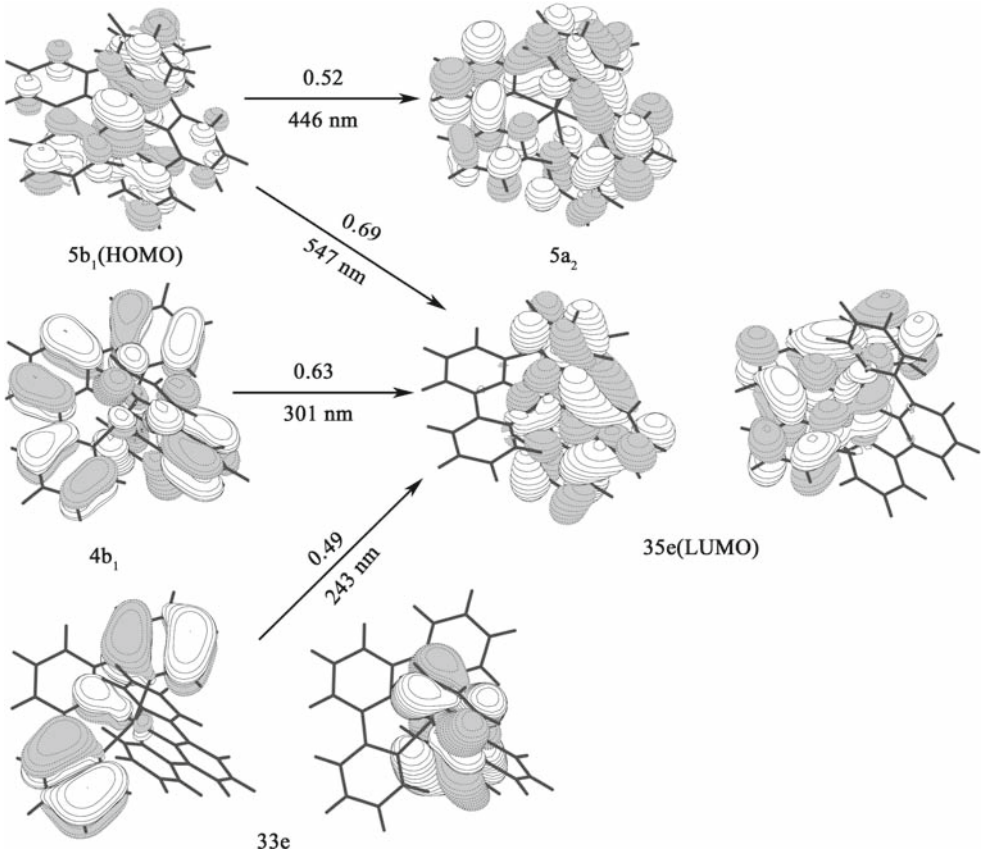

Fig. 2 Single electron transitions with the maximum CI coefficients under TD-DFT calculations for the 547, 446, 301 and 243 nm absorptions of $[Os(tpy\text{-}H)_2]^{2+}$(**1**) in acetonitrile

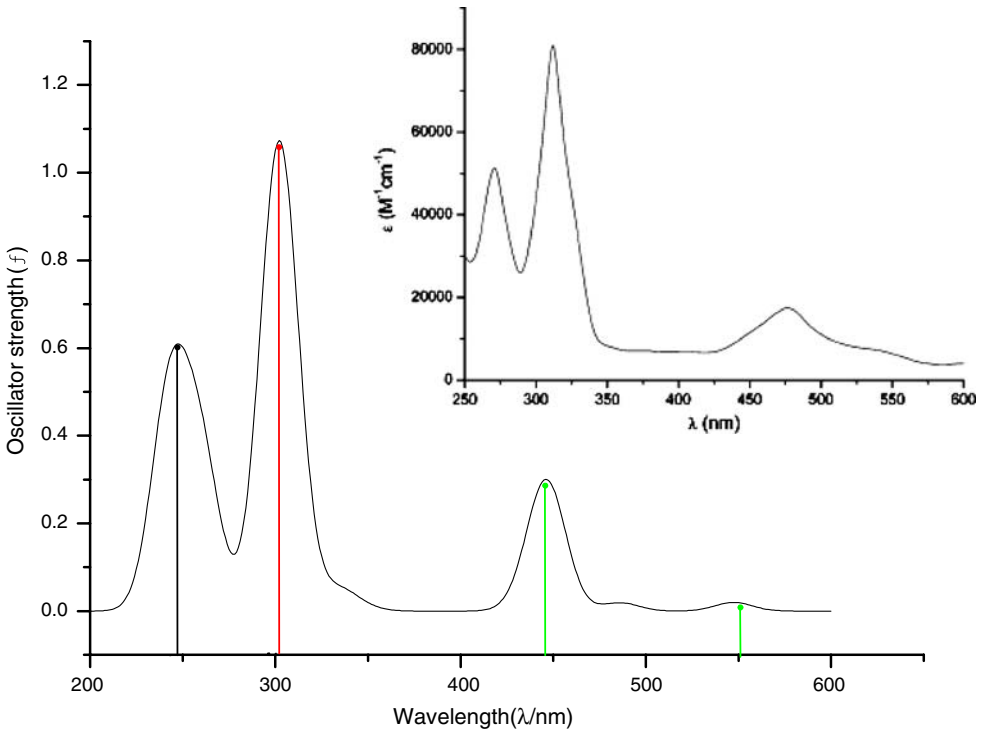

Fig. 3 Simulated absorption spectra with Gaussian curve based on the data calculated under the TD-DFT method in acetonitrile for $[Os(tpy\text{-}H)_2]^{2+}$(**1**). (Excited states listed in Table 2 are colored. *Green lines*: MLCT/ILCT transition. *Red line*: ILCT/LMCT transition. *Black line*: LLCT/LMCT transition.) *Inset*: experimental spectra [45]

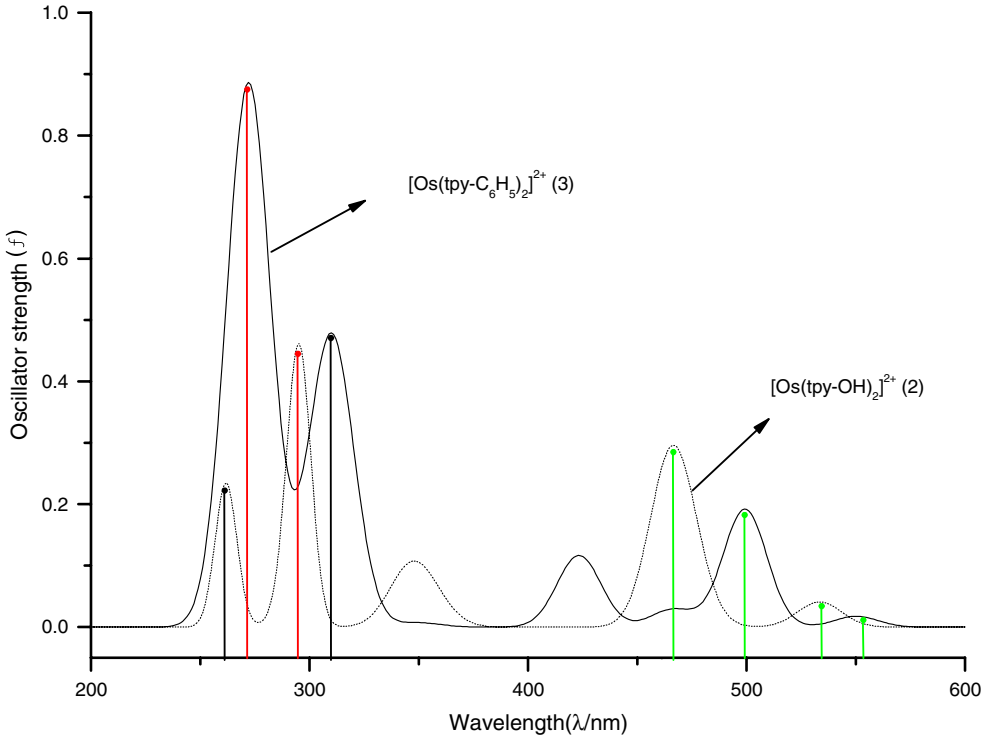

Fig. 4 Simulated absorption spectra with Gaussian curve based on the data calculated under the TD-DFT method in acetonitrile for $[Os(tpy\text{-}OH)_2]^{2+}$(**2**) and $[Os(tpy\text{-}C_6H_5)_2]^{2+}$(**3**). (Excited states listed in Table 2 are colored. *Green lines*: MLCT/ILCT transition. *Red line*: ILCT/LMCT transition. *Black line*: LLCT/LMCT transition.)

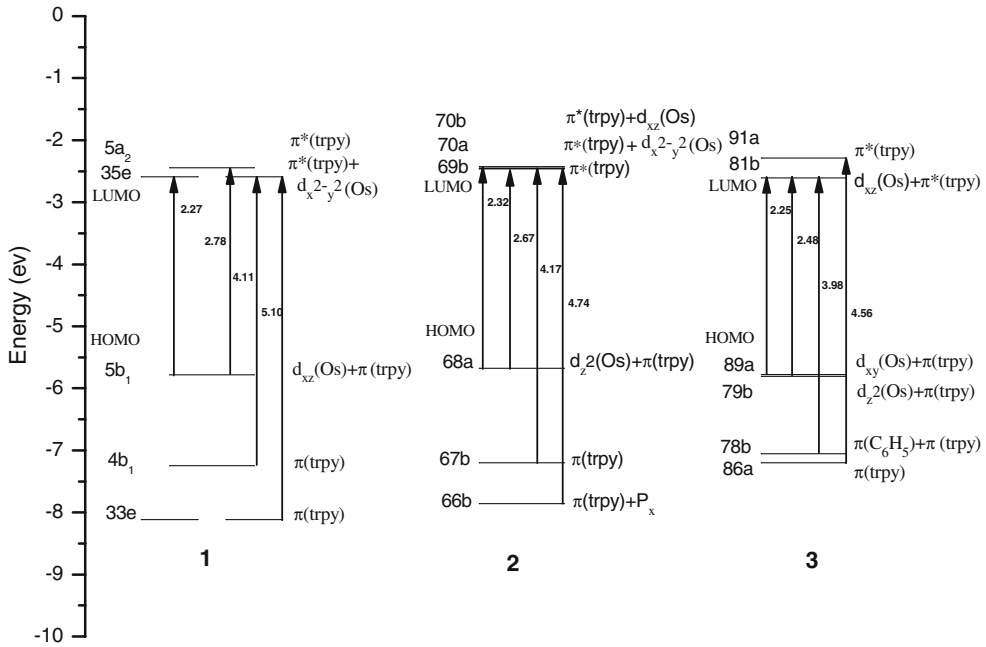

Fig. 5 Diagrams of energy levels of orbitals involved in the absorptions for $[Os(tpy\text{-}H)2]^{2+}$ (**1**), $[Os(tpy\text{-}OH)2]^{2+}$ (**2**), and $[Os(tpy\text{-}C6H5)2]^{2+}$ (**3**) under TD-DFT calculations

the above discussion explicitly. For example, with respect to the 301 nm absorptions, the electron density diagram shows that the charges transfer located on the terpyridyl ligand is attributed to intraligand charge transfer (ILCT) transition

within mixed with some ligand-metal charge transfer (LMCT) characters.

Additionally, for third-row heavy metal (including Os), the strong spin-orbit coupling effectively promotes an intersystem crossing from singlet excited states to lower triplet emitting states [65,66]. The Spin-orbit coupling constants of Osmium and Ruthenium are 3,381 and 1,042 cm^{-1} have been reported [67]. The large spin-orbit coupling of the Os atom enables the spin-forbidden absorptions to be observed in the experimental for the Os-terpy complexes. Therefore, the triplet excited states related to the spin-forbidden absorptions are also considered in the TD-DFT calculations for **1–3**. The lowest-energy absorptions of **1–3** are 667, 680, and 694 nm, respectively, compared with the experimental weak absorption peak at 670 nm.

To analyze the absorption spectra of **2** and **3**, we list their corresponding compositions of frontier orbitals in Tables 4 and 5. As seen in the Tables, unoccupied MOs are dominated by π-antibonding located upon the terpyridyl ligand, while occupied MOs are delocalized on the Os(II) atom, terpyridyl ligand and its substituents. The introduction of the electron-donating substituents into the terpyridyl ligand results in the relevant difference in the compositions of the occupied frontier orbitals of **2** and **3**, which are compared with **1**.

With respect to **2** and **3**, the two lowest-lying absorptions are calculated at 533 and 465 nm for **2** and 550 and 499 nm for **3**, respectively. As seen in Tables 4 and 5, the MO 68a (HOMO-2) of **2** involves 64.3% Os(II), and 33.6% trpy group, while the MOs 89a (HOMO) and 80b (HOMO-1) of **3** comprise 67.2% Os(II), 32.5% trpy and 59.6% Os(II), 33.8% trpy, respectively. The LUMO and LUMO+1 of **2** and LUMO of **3** are a set of quasi orbitals, which are localized on the π orbital of terpyridyl above 83%. Thus, both of the two lowest-lying absorptions of **2** and **3** are all assigned to MLCT mixed with some ILCT transition. It shows that both the oscillator strength and transition properties of the lowest-energy absorptions of **2** and **3** are similar to those of **1**, except of some red shift of the wavelengths. As with the aid of Table 2, one can know that the C^1B excited state of **2** and D^1A excited state of **3** original from the 67b → 70a and 86a → 91a transitions, which have the largest oscillator strength of 0.2573 and 0.7933, respectively, are assigned to the ILCT transition mixed with some ligand-metal charge transfer transition. The corresponding absorptions are located at 297(**2**) and 272(**3**) nm with some blue shift compared with 301 nm of **1**. For the lower-energy 272 nm absorption of **3**, the oscillator strength of 0.79 is far larger than that of corresponding lower-energy absorption of **1** and **2**. The possible reason can be rationalized the presence of the strong resonance between electron-donating phenyl group and terpyridyl ligand.

Additionally, for the 261 and 312 nm absorptions of **2** and **3**, which come from the $X^1A_1 \rightarrow D^1B$ and $X^1A_1 \rightarrow C^1A$ transition, respectively, the 66b → 70a and 78b → 81b excitation configurations corresponding to the largest CI coefficient of 0.34 and 0.49 dominate the absorptions. The occupied MOs 66b and 78b are mainly located on the terpyridyl and its substituents. Therefore, the absorptions with the larger oscillator strength (0.15 and 0.18) of **2** and **3**, are characterized as the LLCT/LMCT transitions perturbed with the LLCT transition arising from a $\pi\pi$ stacking interaction between terpyridine and its substituents. The electron-donating groups connected with the terpyridyl ligand directly affect the occupied molecular orbitals, which lead to the changes of transition properties.

3.2 Substituent effects on absorption spectra

To probe the nature of the substituent effects on absorption spectra, on the basis of the calculated excited states with $f > 0$, we simulated the absorption spectra of **1–3** with Gaussian curves. The fit absorption curves are depicted in wavelength versus oscillator strength in Figs. 3 and 4. The full width at half-maximum of each Gaussian curve is evaluated to be 10 nm based on the narrowest peak of absorption of $[\mathbf{Os}(\text{trpy-H})_2]^{2+}$ in acetonitrile at room temperature [43]. Because the narrowest peak of absorption of terpyridyl Os(II) complexes always arises from the ligand-centered (LC) transition involved in the terpyridine, the selection of the full width is appropriate for **1–3**.

As illustrate in Fig. 3, both the theoretical and experimental absorption spectra of complex **1** are given for comparison. The shapes of the absorption spectra are similar to each other for **1–3**. To intuitively understand the absorptions of **1–3**, we show the various transitions by using colored line (Green line: MLCT/ILCT transition. Red line: ILCT/LMCT transition. Black line: LLCT/LMCT transition). The results show that the MLCT/ILCT(green line) and LLCT/LMCT(Black line) are red-shifted and the ILCT/LMCT(red line) are blue-shifted for **1–3**. The lowest-energy green line demonstrates that the MLCT transitions in these kinds of Os(II) complexes dominate the low-energy absorption. We think that this is the most fascinating factor for the complexes as the emissive candidates. On one hand, this kind of transition is dipole-allowed; on the other hand, the singlet-triplet transition probably occurs due to the participation of the metal. Both of these two properties can ensure the high luminescence efficiency of the complexes [68].

To further shed light on how substituents affect the electronic transitions, the orbital energy levels for **1–3** are illustrated in Fig. 5. It is clearly shown that MLCT/ILCT transitions are red-shifted because the occupied molecular orbitals are sensitive to the variation of substituents. In view of comparing the ability of the electron-donating groups of C_6H_5- and -OH, we calculated their natural charge based on the Natural Bond Orbital (NBO) analysis. The results show that the total charge of the C_6H_5- is 0.06881e, while that of

Table 6 Phosphorescent emissions of **1–3** in acetonitrile under the TD-DFT(B3LYP) calculations, together with experimental values

[a] From ref. [44]

	Transition	Config(CI coeff)	E, nm (ev)	Assignment	λ_{exptl} (nm)[a]
1	$^3E \rightarrow {}^1A_1$	35e→34e (0.55)	649.41 (1.91)	^{3}MLCT/^{3}ILCT	720
2	$^3A \rightarrow {}^1A_1$	70a →69a (0.48)	656.54 (1.89)	^{3}MLCT/^{3}ILCT	
		70b →68b (0.44)		^{3}MLCT/^{3}ILCT	
3	$^3A \rightarrow {}^1A_1$	81b→80b (0.75)	676.28 (1.83)	^{3}MLCT/^{3}ILCT	

Table 7 Molecular orbital compositions in the excited state for $[Os(tpy\text{-}H)_2]^{2+}$(**1**) at the B3LYP level

Orbital	Composition (%)			
	Energy (eV)	Os	trpy	Assignment of orbitals
$5a_2$	−2.3437		100.0	π^*(trpy)
35e	−2.4820	11.6	88.4	π^*(trpy) + d_{xz}(Os)
HOMO-LUMO energy gap				
5b1	−5.7408	71.1	28.9	d_{xy}(Os) + π(trpy)
34e	−5.8238	67.0	33.0	d_{xz}(Os) + π(trpy)
$4a_2$	−7.2497		100.0	π (trpy)

the -OH is –0.13801e, therefore the strength of the electron-donating group should be C_6H_5- > -OH. The occupied molecular orbital energy levels increase significantly in the order C_6H_5 > -OH > H according to the electron-donating ability of C_6H_5 > -OH > H. However, unoccupied orbital energy levels are changed slightly, resulting in the considerable decrease of energy gap between the occupied molecular orbitals and the unoccupied molecular orbitals.

3.3 The lowest-energy excited-state structures and emission spectra in the CH_3CN solution

On the basis of the optimized ground-state structures, the lowest-energy excited state structures of **1–3** are fully optimized by the CIS method. Upon excitation of **1–3**, the structures still keep similarity with respect to those of the ground states (see Table 1). For **1**, the Os-N(1), Os-N(2), and Os-N(3) bond lengths are slightly elongated ca. 0.02–0.03 Å compared with those in the ground state, while the C-N bond length is somewhat shortened. The analogous trends are also observed in **2** and **3**. The variation of bond lengths corresponds to the electrons being promoted from the Os(II) atom to the terpyridyl ligands and the weakened interaction between Os(II) atom and ligands upon excitation. The evidence suggests that ^{3}MLCT/^{3}ILCT transition should be responsible for the lowest-energy emission.

In view of obtaining convincible emissive energies, based on the excited-state structures optimized by the CIS method, the emission spectra of **1–3** in acetonitrile are calculated by the TD-DFT approach at the B3LYP level associated with the PCM model. The corresponding emissions of **1–3** are listed in Table 6 associated with the emissive energies and transition assignments; the frontier molecular orbital compositions responsible for the emissions are compiled in Tables 7, S1, and S2 for **1–3**, respectively; the intuitive electron transition diagram of the emission is shown in Fig. 6.

The calculated lowest-energy phosphorescence in the acetonitrile solution of **1–3** are at 649, 656, and 676 nm, respectively, the nature of which is assigned to the ^{3}MLCT/^{3}ILCT character. We have presented in the above discussions that the lowest-energy absorptions calculated at 547, 533, and 550 nm also arise from the MLCT/ILCT transition. Since the lowest-energy emissions and absorptions have the same symmetry and transition character for each complexes, the phosphorescent emissions should come from the lowest-energy absorptions. The Stokes shifts between the lowest-energy absorptions and emissions are 0.36 (**1**), 0.43 (**2**), and 0.42 eV (**3**), respectively. The modest shifts are in agreement with the minor change between the ground- and excited-states structures.

The 649 nm emission of **1** is assigned to the phosphorescence arising from $^3E \rightarrow {}^1A_1$ transition. Table 7 shows the partial molecular orbital compositions of **1** for further understanding the emissive state. As seen from Table 7, the unoccupied MOs of LUMO are significantly localized on the terpyridyl ligand above 88% compositions, while the MOs $5b_1$ (HOMO) and 34e are mainly contributed by the Os(II) together with terpyridyl ligands. The analogous trend has been observed from the absorption spectrum of **1**. According to above analysis, the 649 nm phosphorescence is attributed to the ^{3}MLCT (π^*(trpy) → d_{xy}(Os)) transition mixed with some ^{3}ILCT ($\pi\pi^*$) character. The electron density diagrams of **1–3** are shown in Fig. 6. With the aid of the diagram, we can intuitively understand the emissive process from the

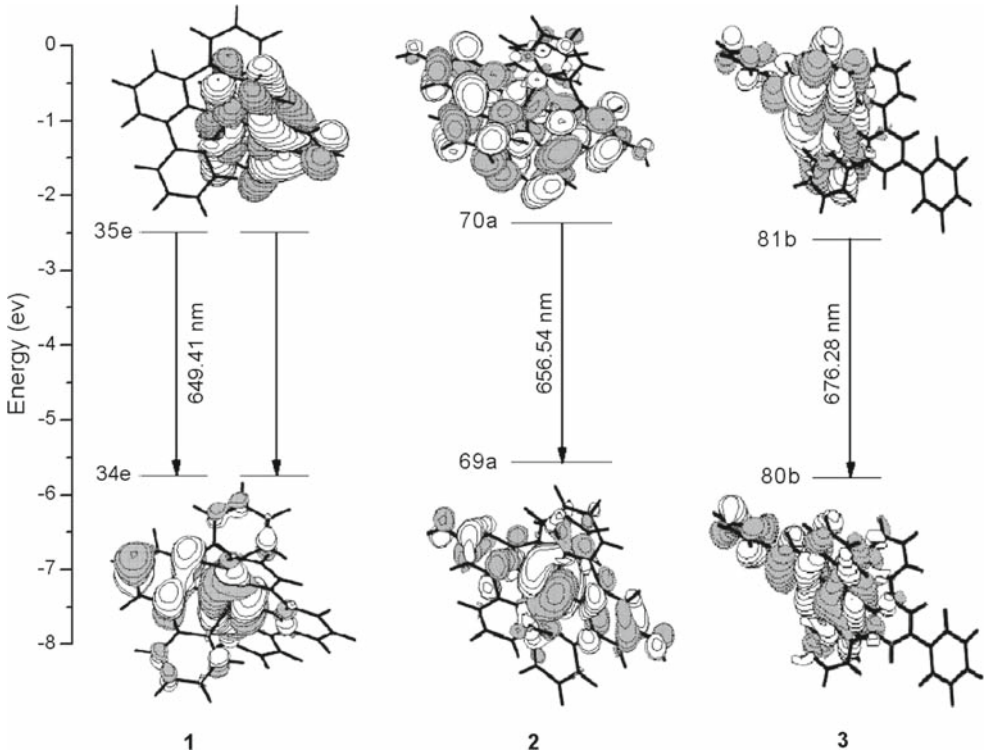

Fig. 6 Transitions responsible for the emissions at 649, 656, and 676 nm for **1**–**3**, respectively, simulated in acetonitrile media

$^3E \rightarrow {}^1A_1$ transition. The MO 35e → MO 34e excitation has the largest configuration coefficient (0.55) and causes the emission. Laine et al. [44] have detected the lowest-energy 724 nm phosphorescence of $[Os(trpy\text{-}H)_2]^{2+}$ in CH_3CN solution at room-temperature. They proposed that ^{3}MLCT transition are responsible to the lowest energy phosphorescence of the complex **1** whatever solutions are used.

Similar to the listing for **1**, the partial frontier orbital compositions of **2** and **3** are listed in Tables S1 and S2, respectively. As depicted in the Tables, unoccupied MOs of **2** and **3** are still localized on the terpyridyl. However, the introduction of -OH and C_6H_5- groups into the terpyridyl ligand results in the difference in the compositions of occupied orbitals on going from **1** to **2** and **3**. The -OH and C_6H_5- groups have little effect to compositions of the first three occupied orbitals, which contribute the MOs below HOMO-5 in **2** and HOMO-3 in **3**, respectively. Therefore, the phosphorescences at 656 nm of **2** and at 676 nm of **3** originating from the $^3A \rightarrow {}^1A_1$ transition are essentially attributed to the π^*(trpy) → d_{xy}(Os) and intraligand ($\pi\pi^*$) charge transfer (^{3}MLCT/^{3}ILCT) transition.

The electron transition diagram of the emission is shown in Fig. 6, which shows the excited states corresponding to the largest CI coefficient in the configuration wave function. As shown in the diagram, HOMO-LUMO energy gaps of **1**–**3** decrease in the order 3.26(**1**) > 3.14(**2**) > 3.11(**3**) eV, which is consistent with the electron-donating ability of the substituent groups C_6H_5 > -OH > H. Moreover, the introduction of substituents causes a red shift of phosphorescent emission on going from **1**–**3**. From the above analysis, it can be anticipated that the excitation energy related to emission will be decreased further, when the electron-donating ability of ligand on terpyridyl is stronger than that of C_6H_5- group.

4 Conclusions

The B3LYP and CIS methods were carried out to optimize the ground and excited state structures of **1**–**3**. On the basis of the optimized structures, the absorption and emission spectra in the CH_3CN solution were obtained by the TD-DFT method associated with the PCM model, respectively. Taking into account the variation of substituents on terpyridine ligand, the following conclusions can be drawn.

Complexes **1**–**3** have similar structures in both the ground and excited states with the variation of the substituents on terpyridine ligand. The minor change of structures between the ground and excited states results in the little stokes shift between the lowest-energy absorption and emission of **1**–**3**.

The lowest-energy absorptions are attributed to the MLCT/ILCT character, whereas the lowest-energy emissions originate from the ^{3}MLCT/^{3}ILCT transitions. When the electron-donating substituents are introduced into the terpyridine

ligand: (1) the lowest-lying absorptions and emissions are red-shifted in the order **1** < **2** < **3**; (2) the higher-energy ILCT transition around 290 nm is blue-shifted contrarily; (3) the substituent effect on occupied molecular orbitals is more significant than that on the unoccupied molecular orbitals.

We hope these theoretical studies can provide some help in designing other $[Os(trpy)_2]^{2+}$complexes.

Acknowledgments This work is supported by the Natural Science Foundation of China (Grant Nos. 20573042, 20333050, and 20173021).

References

1. Paris JP, Brandt WW (1959) J Am Chem Soc 81:5001
2. Demas JN, Crosby GA (1968) J Mol Spectrosc 26:72
3. Hager GD, Crosby GA (1975) J Am Chem Soc 97:7031
4. Hager GD, Watts RJ, Crosby GA (1975) J Am Chem Soc 97:7037
5. Hipps KW, Crosby GA (1975) J Am Chem Soc 97:7042
6. Houten JV, Watts R J (1976) J Am Chem Soc 98:4853
7. Meyer TJ (1983) Prog Inorg Chem 30:389
8. Caspar JV, Meyer TJ (1983) J Phys Chem 87:952
9. Juris A, Balzani V, Campagna PB, Zelewsky AV, Coord (1988) Chem Rev 84:85
10. Yeh AT, Shank CV, McCusker JK (2000) Science 289:935
11. Wrighton M, Morse DL (1974) J Am Chem Soc 96:998
12. Lees A (1987) J Chem Rev 87:711
13. Hsu CC, Cheng YM, Ho ML, Chou PT, Peng SM (2006) Inorg Chem 45:10188
14. Chen YL, Sinha C, Chen IC, Liu KL, Chi Y, Yu JK, Chou PT, Luc TH (2003) Chem Commun 3046
15. O'Regan B, Grätzel M (1991) Nature 353:737
16. Szmacinski H, Lakowicz JR (1995) Sens Actuators B 29:16
17. Castellano FN, Lakowicz JR (1998) Photochem Photobiol 67:179
18. Lakowicz JR, Castellano FN, Dattelbaum JD, Tolosa L, Rao G, Gryczynski I (1998) Anal Chem 70:5115
19. deSilva AP, Gunaratne HQ, Gunnlaugsson T, Huxley AJM, McCoy CP, Rademacher JT, Rice TE (1997) Chem Rev 97:1515
20. Slone RV, Benkstein KD, Belanger S, Hupp JT, Guzei IA, Rheingold AL (1998) Coord Chem Rev 171:221
21. Terpetschnig E, Szmacinski H, Malak H, Lakowicz JR (1995) Biophys J 68:342
22. Guo XQ, Castellano FN, Li L, Lakowicz JR (1998) Anal Chem 70:632
23. Lee JK, Yoo D, Rubner MF (1997) Chem. Mater 9:1710
24. Lyons CH, Abbas ED, Lee JK, Rubner MF (1998) J Am Chem Soc 120:12100
25. Handy ES, Pal AJ, Rubner MF (1999) J Am Chem Soc 121:3525
26. Wu A, Yoo D, Lee JK, Rubner MF (1999) J Am Chem Soc 121:4883
27. Meyer T (1986) J Pure Appl Chem 58:1193
28. Juris A, Balzani V, Barigelletti F, Campagna S, Belser P, vonZelewsky A (1988) Coord Chem Rev 84:85
29. Balzani V, Barigelletti F, De CL (1990) Top Curr Chem 158:31
30. Karvanos GJ (1993) Photoinduced electron transfer. VCH Publishers, New York
31. Collin JP, Guillerez S, Sauvage JP (1989) J Chem Soc Chem Commun 116
32. Constable EC, Cargill Thompson AMW (1992) J Chem Soc Dalton Trans 3467
33. Constable EC, Cargill Thompson AMW, Tocher DA (1993) Supramol Chem 3:9
34. Constable EC, Hawenon P, Smith DR, Whall LA (1994) Tetrahedron 50:7799
35. Kober EM, Marshall JL, Dressick WJ, Sullivan BP, Caspar JV, Meyer TJ (1985) Inorg Chem 24:2755
36. Amouyal E, Mouallem-Bahout M, Calzafem G (1991) J Phys Chem 95:7641
37. Collin JP, Guillerez S, Sauvage JP, Barigelletti F, De CL, Flamigni L, Balzani V (1991) Inorg Chem 30:4230
38. Collin JP, Guillerez S, Sauvage JP, Barigelletti F, De CL, Flamigni L, Balzani V (1992) Inorg Chem 31:4112
39. Grosshenny V, Ziessel RJ (1993) Chem Soc Dalton Trans 817
40. Craig DC, Scudder ML, McHale WA, Goodwin HA (1998) Aust J Chem 51:1131
41. Mauro M, Ja NA, la VB, Ja EC, Constable Jb, Alexander MW, Cargill T (1995) Inorg Chem 34:2159
42. Philippe PL, Fre'de'rique L, Sebastiano C, Ilaria C, Carlo A (2006) Inor Chem 45:5538
43. Ilaria C, Philippe PL, Fethi B, Carlo A (2004) J Am Chem Soc 126:10763
44. Philippe PL, Fethi B, Fre'de'r L, Claudio C, Sebastiano C (2006) J Am Chem Soc 128:7510
45. Ciofini I (2006) Theor Chem Acc 116:219
46. Hammarström L (2003) Curr Opin Chem Biol 7:666
47. Wasielewsky MR (1992) Chem Rev 92:435
48. Baranoff E, Collin JP, Flamigni L, Sauvage JP (2004) Chem Soc Rev 33:147
49. Hagfeldt A, Grätzel M (2000) Acc Chem Res 33:269
50. Bignozzi CA, Argazzi R, Indelli MT, Scandola F (1992) Sol Energy Mater Sol Cells 32:229
51. O'Regan B, Grätzel M (1991) Nature 353:737
52. Zhou X, Ren AM, Feng JK (2005) J Organomettallic Chem 690:338
53. Becke AD (1993) J Chem Phys 98:5648
54. Stanton JF, Gauss J, Ishikawa N, Head-Gordon MJ (1995) Chem Phys 103:4160
55. Foreman JB, Head-Gordon M, Pople A (1992) J Phys Chem 96:135
56. Waiters VA, Hadad CM, Thiel Y, Colson SD, Wibergy KB, Johnson PM, Foresmanl JB (1991) J Am Chem Soc 113:4782
57. Casida ME, Jamorski C, Casida KC, Salahub DR (1998) J Chem Phys 108:4439
58. Stratmann RE, Scuseria GE (1998) J Chem Phys 109:8218
59. Matsuzawa NN, Ishitani A (2001) J Phys Chem A 105:4953
60. Cossi M, Scalmani G, Regar N, Barone V (2002) J Chem Phys 117:43
61. Barone V, Cossi MJ (1997) Chem Phys 107:3210
62. Wadt WR (1985) J Chem Phys 82:284
63. Hay PJ, Hay WR (1985) J Chem Phys 82:299
64. Frisch MJ, Trucks GW, Schlegel HB, Scuseria GE, Robb MA, Cheeseman JR, Montgomery JA, Jr, Vreven T, Kudin KN, Burant JC, Millam JM, Iyengar SS, Tomasi J, Barone V, Mennucci B, Cossi M, Scalmani G, Rega N, Petersson GA, Nakatsuji H, Hada M, Ehara M, Toyota K, Fukuda R, Hasegawa J, shida M, Nakajima T, Honda Y, Kitao O, Nakai H, Klene M, Li, Knox JE, Hratchian HP, Cross JB, Bakken V, Adamo C, jaramillo J, Gomperts R, Stratmann RE, Yazyev O, Austin AJ, Cammi R, Pomelli C, Ochterski JW, Ayala PY, Morokuma K, Voth GA, Salvador P, Dannenberg JJ, Zakrzewski VG, Dapprich S, Daniels AD, Strain MC, Farkas O, Malick DK, Rabuck AD, Raghavachari K, Foresman JB, Ortiz JV, Cui Q, Baboul AG, Clifford S, Cioslowski J, Stefanov BB, Liu G, Liashenko A, Piskorz P, Komaromi I, Martin RL, Fox DJ, Keith T, Al-Laham MA, Peng CY, Nanayakkara A, Challacombe M, Gill, PMW, Johnson B, Chen W, Wong MW, Gonzalez C, Pople JA (2004) Gaussian 03, revision C.02. Gaussian Inc., Wallingford, CT
65. Benniston AC, Harriman A, Li PY, Sams CA (2005) J Phys Chem A 109:2302

66. Yu JK.Cheng YM, Hu YH, Chou PT, Chen YL, Lee SW, Chi Y (2004) J Phys Chem B 108:19908
67. Murov S L, Carmichael I, Hug GL (1993) Handbook of photochemistry. Marcel Dekker, New York
68. Liu T, Xia BH, Zhou X, Zhang HX, Pan QJ, Gao JS (2007) Organometallics 26:143